Author/s:
Chen, D;Rezaei, S;Rosendahl, PL;Xu, BX;Schneider, J

Title:
Multiscale modelling of functionally graded porous beams: Buckling and vibration analyses

Date:
2022-09-01

Citation:
Chen, D., Rezaei, S., Rosendahl, P. L., Xu, B. X. & Schneider, J. (2022). Multiscale modelling of functionally graded porous beams: Buckling and vibration analyses. Engineering Structures, 266, https://doi.org/10.1016/j.engstruct.2022.114568.

Persistent Link:
https://hdl.handle.net/11343/315711

Multiscale Modelling of Functionally Graded Porous Beams: Buckling and Vibration Analyses

Da Chen [1234*], Shahed Rezaei [1], Philipp L. Rosendahl [2], Bai-Xiang Xu [1], Jens Schneider [2]

[1] Mechanics of Functional Materials Division, Department of Materials Science, Technical University of Darmstadt, Germany
[2] Institute of Structural Mechanics and Design, Department of Civil and Environmental Engineering, Technical University of Darmstadt, Germany
[3] Department of Infrastructure Engineering, The University of Melbourne, VIC 3010, Australia
[4] School of Civil Engineering, The University of Queensland, St. Lucia, QLD 4072, Australia
[*] Corresponding author: d.chen@uq.edu.au

Abstract

This paper combines the finite element (FE) homogenisation and structural assessments to conduct the multiscale modelling of laminated functionally graded (FG) porous beams made of closed-cell foams, with a focus on the beam buckling and vibration performances. In the FE homogenisation, representative volume elements (RVEs) are built up according to the relative densities, average cell sizes, and base material properties from foam samples. They are used to predict the foam Young's modulus and verified against existing studies. A detailed investigation is then carried out to disclose the effects of RVE and porosity features, where the relative density is confirmed as the dominating factor in the calculation of foam modulus. Quantitative relations between pore structure and Young's modulus are obtained via data fitting.

In the subsequent structural assessment, the predicted Young's modulus is employed in the buckling and vibration analyses of FG porous beams, which are constructed by a six-layer laminated beam model and consist of high-, medium-, and low-density layers with varying designated relative densities. The Timoshenko beam theory and the Ritz method are applied to derive and solve the governing equations. Convergence and validation studies are performed accordingly to ensure the validity of presented results, followed by a parametric study to examine various FG beams concerning different porosity distributions, boundary conditions, and slenderness ratios. The prominence of graded porosities is evidenced by apparently promoted beam stiffness with over 30% and 10% increments in the critical buckling load and fundamental natural frequency, respectively. The graded porosities can be linked to realistic closed-cell Aluminium foams with developed quantitative relations, shedding important and practical guidance into the porous structural design.

Keywords

Functionally graded porous beams, multiscale modelling, homogenisation, representative volume element, elastic buckling, free vibration.

1. Introduction

Owing to the exceptional volume–to–mass ratio, cellular materials possess high application potential in the lightweight structural components across building, automotive, aerospace, and biomedical industrial sectors [1, 2], of which lattice structures are featured with architected and repeated geometries to provide controllable mechanical properties [1, 3]. Meanwhile, highlighted by random (stochastic) arrangements of open or closed internal pores, cellular foams made of different base materials (such as metals, polymers, and concretes) are an attractive option for various engineering fields with relatively inexpensive manufacturing costs [3]. Particularly, metal foams present unique advantages in producing weight-reduced components for working platforms, crush absorbers for vehicles, heat exchangers, and passive thermal cooling devices, based on their low densities, good stiffnesses, excellent energy absorption capacities, and advanced thermal properties [2, 4, 5]. The commercial production of metal foams is boosted by the growing need of multifunctional materials, leading to a fast-developing emerging market.

Structures made of metal foams are gaining impressive traction in various industries. Recent studies show that a further improvement of their mechanical properties can be rather easily achieved by adjusting the porosity patterns, resulting in the vast development of functionally graded (FG) porous structures [6]. Among the earliest investigators in this field, Magnucki and Stasiewicz [7] conducted a buckling analysis on an FG porous beam and obtained the analytical solutions. Magnucka-Blandzi [8, 9] examined the dynamic stability, axi-symmetrical deflection and buckling of FG circular plates made of open-cell metal foams. Chen et al. [10-13] systematically measured the elastic buckling, static bending, linear free and forced vibration, nonlinear free vibration, and postbuckling behaviours of regular and sandwich porous beams, with a special focus on the performance enhancement induced from non-uniform porosity distributions. They also pointed out that an FG porous core is able to avoid the possible interfacial failure of sandwich structures [14].

The superiorities of FG porous structures are being disclosed and making this novel structural form extremely appealing. Consequently, a booming research effort has been devoted into this field during the past few years. Gao et al. [15] employed the hybrid Chebyshev surrogate model with discrete singular convolution method to investigate the nondeterministic vibration frequencies and mode shapes of FG porous beams, considering the uncertainty in material properties. Wu. et al. [16] introduced an finite element (FE) computation framework for the free and forced vibrations of beams with different porosity distributions, and compared the results from Timoshenko beam theory and Euler-Bernoulli or classical beam theory. Twinkle and Pitchaimani [17] imported the graphene platelets as nanofillers into the design of multilayer cylindrical panels with graded internal pores, of which the buckling and free vibration solutions are exploited in light of a higher order shear deformation theory. Masjedi et al. [18] regarded graded cellular materials as variable stiffness bioinspired materials, and studied the three-dimension (3D) large deflections of FG porous beams according to a geometrically exact model with fully intrinsic formulations under conservative and non-conservative loads. The fabrication strategy of foams with graded porosities has also been actively explored via powder space holder technique [19], sintering and dissolution processing [20], and friction stir processing [21], etc.

Wu et al. [6] reviewed the recent works on the mechanical analysis of FG porous structures and pinpointed the current challenges while highlighting their promising future. One of the three critical challenges listed by them is related to the lack of understanding regarding the dependency of structural performances on cellular geometries. As a matter of fact, most of the above-mentioned papers fail to give a clear connection between the mesoscopic porosity configurations and the overall mechanical responses.

It is well known that the advantages of cellular materials originate from their unique meso-structures [22, 23]. The influence of mesoscopic porosity configurations is significant and commonly evaluated by means of two-dimension (2D) or 3D FE simulations [24-26]. However, the corresponding research on FG porous geometries is rather scarce and mainly focused on the crushing simulation. Chen et al. [27] developed FG porous structures with different distributions and compared their energy absorptions under varying impacts. Zhang et al. [28] analysed the dynamic behaviour of FG aluminium foam-cored sandwich beams subjected to shock impulses by using full-scale FE models. Liang et al. [29] theoretically and numerically investigated the blast responses of density graded cellular bars to clarify the effects of the gradient distributions and variations.

To address this urgent challenge, we employ multiscale modelling techniques to link the structural macroscopic buckling and vibration behaviours with the detailed mesoscopic graded porosity features, such as cell sizes and cell wall thicknesses. This linkage is vitally important to provide industries concrete instructions on the manufacturing of FG porous components with better buckling and vibration resistance, and paves the way for the fast commercialisation of this new structural form. Specifically, a laminated beam is developed in this paper and contains different layers with closed-cell foams of varying porosities, leading to changing elastic moduli across the beam thickness. The foam Young's moduli are obtained via FE computational homogenisation, where a 2D representative volume element (RVE) model is proposed to mimic the meso-structures of closed-cell geometries. 655 RVE cases are computed in total to comprehensively reveal the influence of various porosity parameters. The critical buckling loads and fundamental natural frequencies of FG porous beams are determined thereafter, and connected to the detailed features of Aluminium foams, providing the much-needed linkage between cellular geometries and structural performances. Our findings may be applied in the fabrication of lightweight stiff components in sliding beds and textile machines, vehicle and aircraft frames, and crane working platforms, etc.

2. FE Homogenisation of closed-cell foams

The multiscale modelling in this study is divided into two parts: FE homogenisation of closed foams in section 2 for the mesoscopic analysis on cellular geometries, and FG beam assessments in section 3 for the macroscopic calculation on overall structural responses. These two sections are interconnected with the foam Young's modulus which is first obtained based on detailed cellular geometries with RVEs in section 2, and then is used as a primary property in the buckling and vibration examinations of FG beams in section 3. Thus, the buckling load and natural frequency of beam components can be linked to mesoscopic porosity features, such as average cell size and cell wall thickness, via the foam Young's modulus.

Concretely speaking, section 2 starts with RVE construction (section 2.1) and validation (section 2.2). Then RVE parametric studies (section 2.3) are presented to build up a solid basis for data fitting (section 2.4), leading to the determination of quantitative relations between porosity features and foam Young's modulus for the beam structural analysis in section 3.

2.1. RVE construction

Based on the micromechanics theory, an RVE can be defined for a heterogeneous microstructural sample, assuming that the RVE is statistically representative in terms of the characteristics for the whole porous structure. FE homogenisation can be then carried out on the RVE to evaluate the mesoscopic property of materials made of complex microstructures. This method has been successfully applied for various microstructures in different fields [30-33]. It is also promising for studying the mechanical properties of cellular materials and particularly metal or polymer foams, as shown in [22, 34-36]. The Voronoi tessellation with convex cells has been demonstrated to be an effective approach for the internal porosity construction [26, 27], especially for high-porosity closed-cell Aluminium foams with polyhedral cell configurations [37, 38]. Therefore, this paper adopts Voronoi techniques to generate porous geometry details (such as cell positions, cell wall lengths, etc.) by using MATLAB (version: R2021a), which are then imported into ANSYS/APDL (version: 2020 R2) to build up the corresponding 2D RVE FE models. This workflow system allows for a fast examination on large amounts of various RVEs at a relatively low computational cost. Note that the seed positions of Voronoi cells are based on randomly sampled numbers from the standard uniform distribution with a constant probability distribution function.

As illustrated in Fig. 1, the proposed square RVE (size: H_{RVE}^{2} mm^2) is enclosed by periodic wavy edges to meet the implementation requirement of periodic boundary conditions (PBCs). A Cartesian coordinate system is established with x and y denoting the horizontal and vertical axes, respectively, and its origin point is located at the square centre. Except for those along four edges (example cells along the top edge are highlighted in Fig. 1) which are positionevenly distributed, all internal cells are randomised in terms of positions, sizes, and shapes. Cell walls with a uniform thickness t_{wall} are represented by straight beams connected rigidly, where a Timoshenko beam element (BEAM188) is employed to account for the shear deformation effects and is featured with a square cross section (beam element thickness = cell wall thickness). To ensure accurate simulations with beam elements, a minimum cell wall length ($\approx 3t_{wall}$) is applied. This strategy is similar to introducing a Matern-Hardcore-radius in the Voronoi tessellation as it was done in [39, 40]. Regarding the edge supports, to connect the movements of corresponding node pairs on opposite edges, PBCs are implemented both vertically and horizontally: vertical PBCs for Δx on top/bottom edges and horizontal PBCs for Δx and Δy on left/right edges, i.e., the movements of top/bottom edge node pairs remain equivalent horizontally, while those for left/right edges are coupled in both directions. Meanwhile, the bottom-edge nodes ($y = -H_{RVE} / 2$) are constrained with $\Delta y = 0$ and a vertical movement of top-edge nodes ($y = H_{RVE} / 2$) is defined as $\Delta y = -H_{RVE} \cdot 1\%$. In addition, all the nodal movements in out-of-plane directions are zero, and those of four corner nodes are limited by $\Delta x = 0$ to avoid rigid-body displacements.

We next perform Static Structural Analysis on constructed RVEs and identify their vertical reaction force F_y under compression for the computation of Young's modulus:

$$E_{RVE} = \left| \frac{F_y / \left(H_{RVE} \cdot t_{wall} \right)}{\Delta y / H_{RVE}} \right| \tag{1}$$

which is assumed to be the same for the whole foam component in order to conduct the overall performance examination. Since this system is solved linearly to only consider small deformations, E_{RVE} do not vary with different compressive strains.

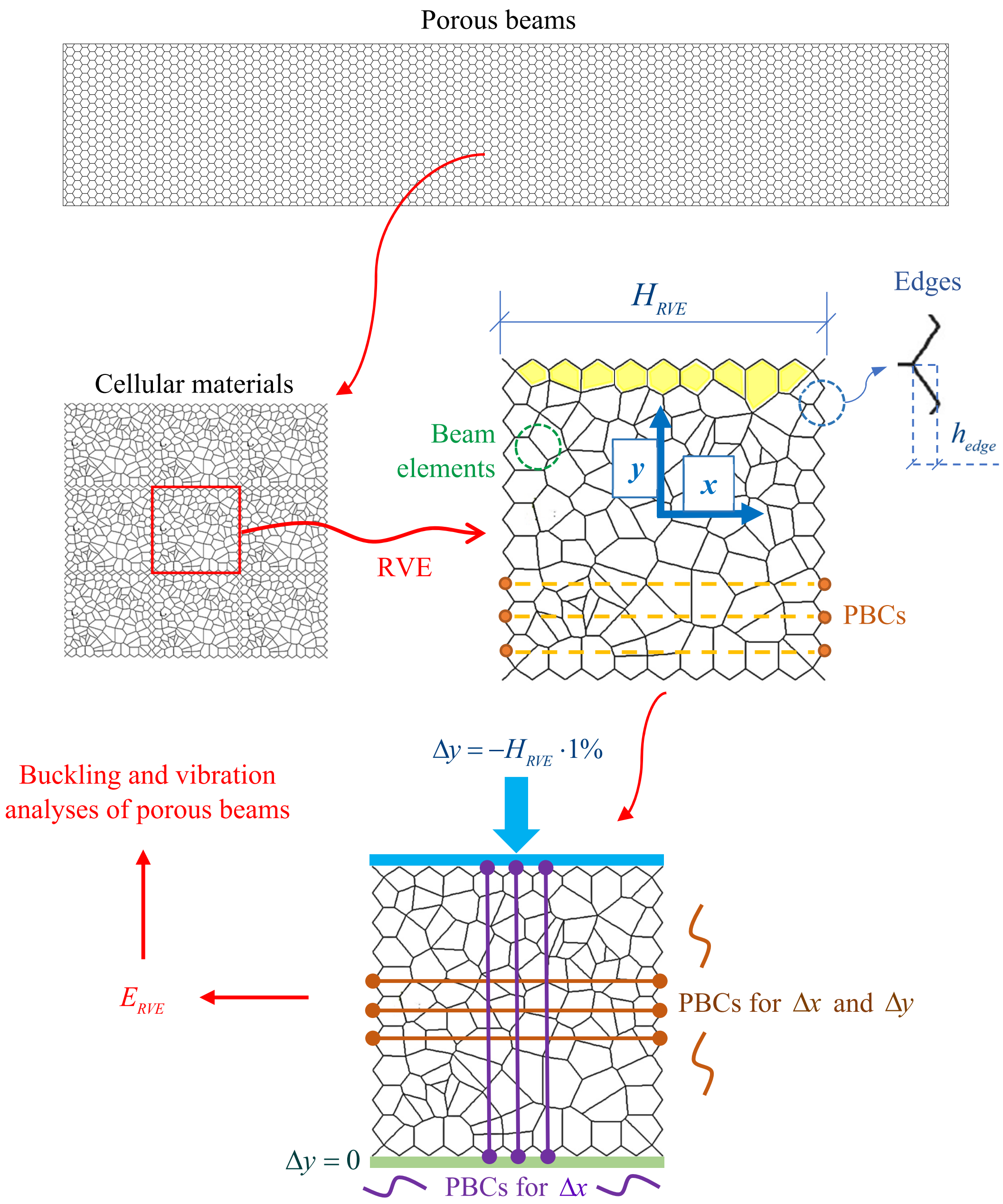

Fig. 1. Illustration of RVE construction and calculation.

The linkage between proposed RVEs and cellular materials in reality is vital. To provide practical design guidelines, we adopt an average cell size d_{cell} (average cell area $\pi\left(d_{cell}/2\right)^2$ for counting cell numbers [41]) and a relative density α from foam products as the key porosity features in the RVE construction. These two parameters are commonly employed in the related research and industry reports, and used herein to estimate the total RVE cell number N_{RVE}:

$$N_{RVE} = n_{cell} + n_{edge} \approx \frac{H_{RVE}^2 \cdot (1-\alpha)}{\pi \left(d_{cell}/2\right)^2} \tag{2}$$

where α (relative density) is the ratio between foam density and the base material density, n_{cell} is the number of cells inside of RVE edges, n_{edge} denotes the average number of cells formed by adjacent edges of neighbouring RVEs and $n_{edge} = 2\Psi$ (Ψ is the smallest even number larger than H_{RVE}/d_{cell}). For instance, $n_{edge} = 20$ for the RVE model in Fig. 1 with 10 external cells formed on each edge, and each cell is shared between two adjacent RVEs. The edge thickness h_{edge} (see Fig. 1) varies within the range of $\left(26\% \sim 40\%\right) d_{cell}$ according to the RVE size, average cell size, and edge cell number. Its influence may be ignored, as per the parametric study in section 2.3. This is due to the fact that compared to the edges, the internal porous structure inside of RVEs is the primary load-carrying component to determine the overall Young's modulus.

The obtained cell numbers are used in the construction of random porosity configurations in a H_{RVE}^2 square field with the aid of Voronoi tessellation and standard uniform distribution. The total cell wall length L_{wall} can be calculated based on each configuration, and the corresponding cell wall thickness t_{wall} reads

$$t_{wall} = \frac{H_{RVE}^2 \cdot \alpha}{L_{wall}} \tag{3}$$

Note that the overlapping of beam elements with centre lines crossing the same joint is assumed to be negligible against the overall RVE volume, hence not considered in Eq. (3).

2.2. RVE validation

In order to verify the effectiveness of presented RVE formulations, two validation cases are given in this paper to compare the obtained Young's moduli against those from experimental studies in open literature. Case A is focused on closed-cell aluminium foams (ALPORAS, widely researched [42-44]) and Case B examines closed-cell polymer foams (Rohacell® 51 WF), of which the base materials are Al-Ca-Ti Aluminium alloy and Polymethacrylimide (PMI), respectively. The average cell sizes, relative densities, and base material properties of foam samples are employed to build up the corresponding RVE models. The external dimensions of samples are not required to be exactly mimicked as long as the RVE contains sufficient internal cells to reflect representative features. It is because repeatable properties can be achieved when RVE models are large enough, despite the randomised porosity geometries (evidenced by the results in section 2.3.1).

Tables 1 and 2 tabulate the details of two validation cases and the employed RVE models are depicted in Fig. 2. Table 3 compares Young's moduli of foam samples and the present results from RVE models, where a good agreement is reached for Aluminium foams which are used in the following analysis, while a larger gap is revealed for polymer foams. This may be explained by the uneven cell wall thickness in foam samples and can also be related to the specific manufacturing method. In the FE simulations of RVE models, the mesh density is controlled with ANSYS Smart Size Feature and the size level is set as 1 (fine mesh). Its validity is verified in a mesh sensitivity analysis, elaborated in Table 4.

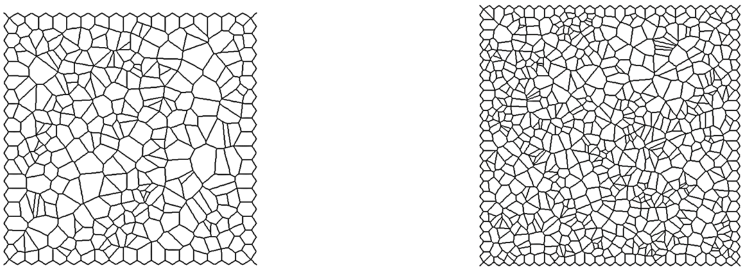

(A) Model A (B) Model B

Fig. 2. RVE models used as validation cases.

Table 1

Validation case A: closed-cell Aluminium foams (ALPORAS).

	Foam sample A [42]	**RVE model A (Fig. 2A)***
Dimensions	50 × 50 × 30 mm^3	H_{RVE}^2 ($H_{RVE} = 50$ mm)
Porosity features		
Average cell size d_{cell}	2.88 mm	2.88 mm
Cell number N_{RVE}		351 (Eq. (2))
Relative density α	8.52% ± 0.74%**	8.52%
Total cell wall length L_{wall}		1854.3 mm
Cell wall thickness t_{wall}		0.1149 mm (Eq. (3))
Base material properties		
Young's modulus	61.7 GPa	61.7 GPa
Mass density	2700 kg/m^3	2700 kg/m^3
Poisson's ratio	0.3	0.3

*RVE edge setting: $n_{edge} = 36$, $h_{edge} = 0.8723$ mm.

** Relative density = (230 ± 20) / 2700 [42].

Table 2

Validation case B: closed-cell polymer foams (Rohacell® 51 WF).

	Foam sample B [43]	**RVE model B (Fig. 2B)***
Dimensions	~Ø24.8 × 26.7 mm	H_{RVE}^2 ($H_{RVE} = 10$ mm)
Porosity features		
Average cell size d_{cell}	0.4 mm	0.4 mm
Cell number N_{RVE}		761 (Eq. (2))
Relative density α	4.4% ± 0.1%	4.4%
Total cell wall length L_{wall}		547.1 mm
Cell wall thickness t_{wall}		0.00804 mm (Eq. (3))
Base material properties		
Young's modulus	5.2 GPa	5.2 GPa
Mass density	1416 kg/m^3	1416 kg/m^3
Poisson's ratio		0.3 [45]

* RVE edge setting: $n_{edge} = 52$, $h_{edge} = 0.1346$ mm.

Table 3

Young's moduli (MPa) of foam samples and RVE models.

	Aluminium foam (case A)	**Polymer foam (case B)**
Foam sample	1100 ± 100 [42]	50* [43]
RVE model (Fig. 2)	1065.20 (Model A, Eq. (1))	45.37 (Model B, Eq. (1))

* Initial elastic modulus.

Table 4
Mesh sensitivity analysis on RVE models.

		Element size (mm)	Node number	Young’s modulus (MPa)
Aluminium foam (case A)	Mesh cases	1.00	1982	1065.20
		0.50	3881	
		0.25	7565	
	Present	Smart Size (1)	4929	
Polymer foam (case B)	Mesh cases	0.2	3200	45.37
		0.1	5884	
		0.05	11257	
	Present	Smart Size (1)	13037	

2.3. Parametric studies on RVEs

The following discussions and calculations in this paper are based on the validation case A (closed-cell Aluminium foams). In this section. various RVEs with different external sizes and randomised internal porosity configurations are examined first. The effects of cell wall thickness, average cell size, and relative density on Young’s moduli are subsequently revealed. 655 RVE cases are investigated here, providing a sound basis for the data fitting in section 2.4. From a statistical point of view, the coefficient of variation is used to identify the relative dispersion of target data points with respect to the mean value, and can be written as

$$\xi = \frac{S}{\overline{X}} \tag{4}$$

where the population standard deviation S reads

$$S = \sqrt{\frac{\Sigma\left(X_i - \overline{X}\right)^2}{N}} \quad (i = 1, 2, \cdots, N) \tag{5}$$

of which X_i represents each data point, $\overline{X}$ denotes the mean value, and N is the population size.

2.3.1. Different RVE external sizes and porosity configurations

Fig. 3 illustrates five RVE external sizes discussed in this paper, involving 30^2, 40^2, 50^2, 60^2, and 70^2 mm^2, where five random porosity configurations are generated for each size (those for 30^2 mm^2 are given in Fig. 3), leading to a total of 25 cases, as tabulated in Table 5. All these models share the same average cell size (2.88 mm), relative density (8.52%), and the base material properties of Aluminium foams in Table 1. We can find that the cell wall thickness and total cell wall length vary among porosity configurations, while the changes are less than 2% under the same H_{RVE}. Different edge settings are also adopted and shown in Table 5. The obtained Young's moduli are disclosed in Fig. 4, and located in the suggested range (1100 ± 100 [42]) with a small coefficient of variation ($\xi = 2.45\%$, $\bar{X} = 1060.90$ MPa, $S = 26.01$ MPa), indicating that the external size, porosity configuration, and edge setting do not exert an evident influence. Therefore, in light of the computational cost, $H_{RVE} = 50$ mm is selected for the following discussions.

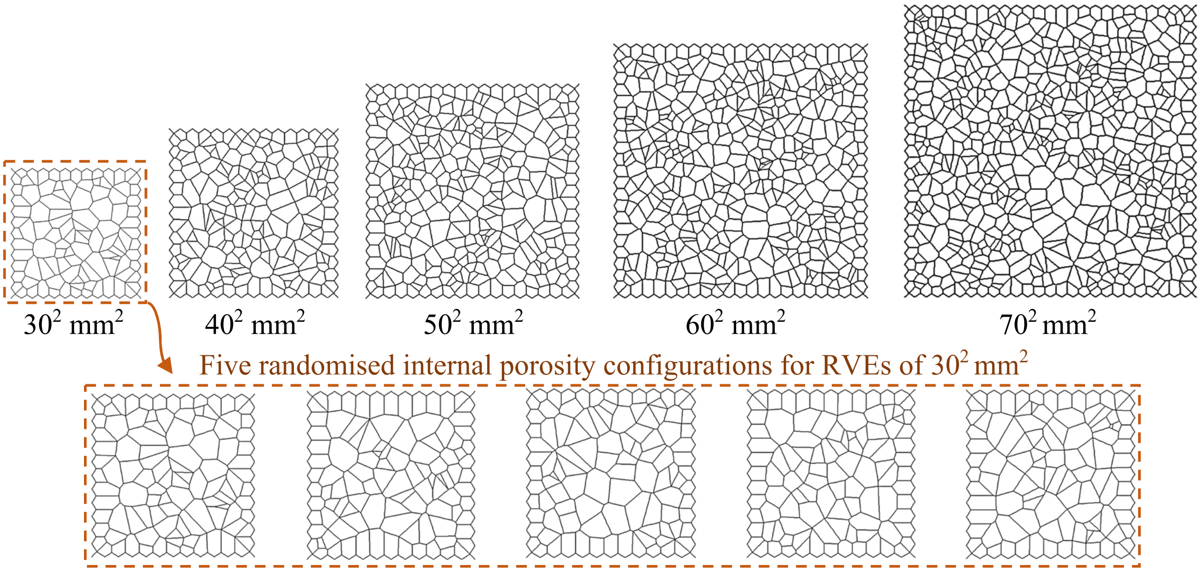

Fig. 3. RVEs with different external sizes.

Table 5

RVE cases with different external sizes and internal porosity configurations.

Size H_{RVE}^2 (mm^2)	**Cell number** N_{RVE}	**Edge setting**		**Case**	**Cell wall thickness** t_{wall} (mm)	**Total cell wall length** L_{wall} (mm)
		n_{edge}	h_{edge} (mm)			
30^2	126	24	0.7870	1.1	0.1168	656.8
				1.2	0.1174	653.0
				1.3	0.1170	655.2
				1.4	0.1175	652.3
				1.5	0.1165	657.9
40^2	225	28	1.0074	2.1	0.1148	1187.3
				2.2	0.1141	1195.4
				2.3	0.1148	1188.0
				2.4	0.1158	1177.1
				2.5	0.1149	1186.6
50^2	351	36	0.8723	3.1	0.1149	1854.3
				3.2	0.1151	1850.0
				3.3	0.1152	1849.2
				3.4	0.1149	1854.0
				3.5	0.1147	1857.8
60^2	506	44	0.8557	4.1	0.1144	2680.4
				4.2	0.1158	2647.5
				4.3	0.1148	2671.8
				4.4	0.1142	2686.2
				4.5	0.1153	2658.9
70^2	688	52	0.9425	5.1	0.1150	3629.1
				5.2	0.1147	3638.8
				5.3	0.1148	3637.1
				5.4	0.1146	3644.2
				5.5	0.1150	3628.8

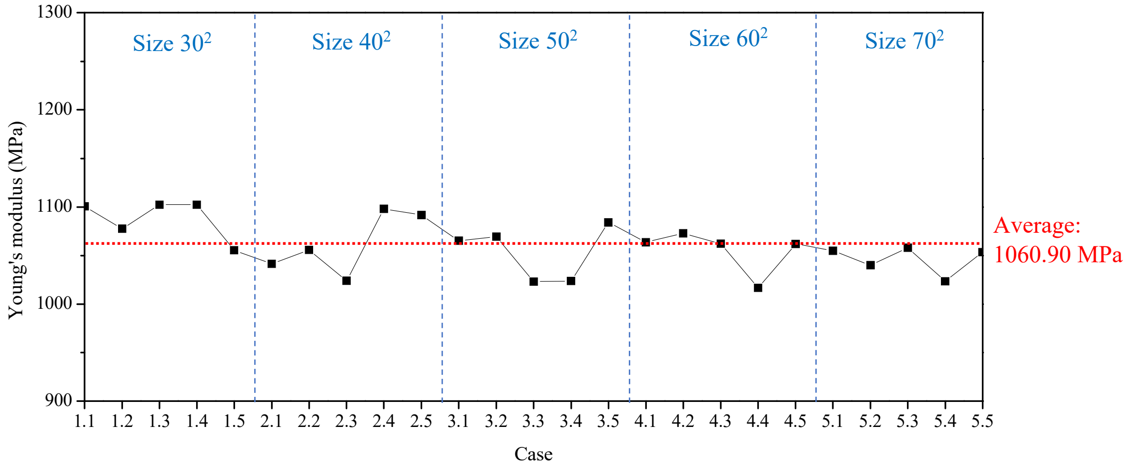

Fig. 4. Young's moduli of RVE cases in Table 5.

2.3.2. Different loading scenarios

Fig. 5 presents two loading scenarios for proposed RVEs, in which aforementioned studies are applied by scenario I with the corresponding details listed in section 2.1. In scenario II, the node pairs on top/bottom edges share the same horizontal and vertical movements (PBCs for Δx and Δy), while those on left/right edges move equivalently only in the vertical direction (PBCs for Δy). Meanwhile, the nodes on the left edge ($x = -H_{RVE} / 2$) are supported by $\Delta x = 0$, and a horizontal nodal movement $\Delta x = -H_{RVE} \cdot 1\%$ is imposed on the right edge ($x = H_{RVE} / 2$). Moreover, four nodes on the RVE corners are restricted with $\Delta y = 0$, i.e., no rigid-body movement. Cases 3.1 ~ 3.5 in Table 5 are reevaluated under Loading scenario II for a direct comparison with the predictions from Loading scenario I, as shown in Table 6 where a close match is found especially between the mean values from two scenarios. It should also be mentioned that high deformations are basically concentrated on the same cell wall components for a specific porosity configuration under both scenarios. Hence, load scenarios do not markedly affect the RVE results, and scenario I is thereby continuously employed in the subsequent analysis.

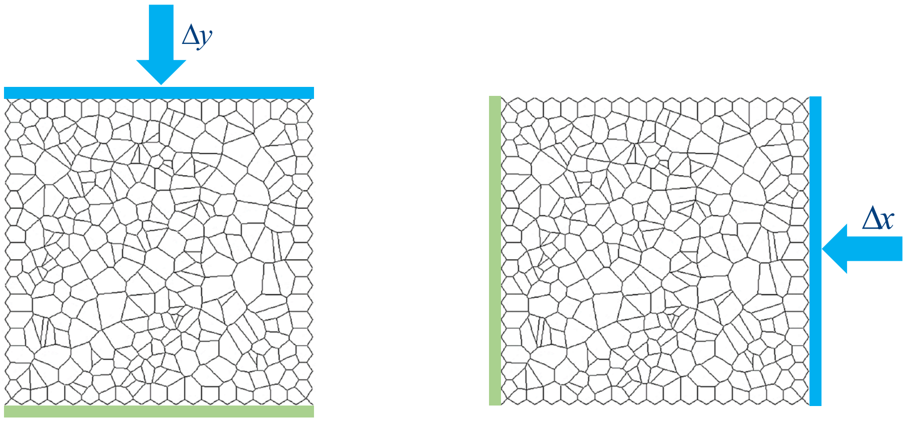

(A) Loading scenario I (B) Loading scenario II

Fig. 5. RVE loading scenarios.

Table 6

RVE Young's moduli under different loading scenarios.

Case (Table 5)	**Loading scenario I (Fig. 5A)**	**Loading scenario II (Fig. 5B)**
3.1	1065.20	1052.78
3.2	1069.62	1078.66
3.3	1023.00	1002.47
3.4	1023.75	1026.01
3.5	1084.24	1089.32
Mean	1053.16	1049.85

2.3.3. Same relative density

This section assumes variations in average cell size and cell wall thickness to examine their effects on the foam Young's modulus under the same relative density of 8.52% (validation case A, $H_{RVE} = 50$ mm). The average cell size is successively raised from 2.5 mm to 5.5 mm (in the realistic cell size range [42]) with an increment of 0.1 mm while the edge settings are adjusted accordingly and detailed in Table 7. Three corresponding examples of RVE models are described in Fig. 6. Results of five different porosity configurations are averaged for each cell size, leading to a total of 155 calculation cases in this section.

Table 7

RVE Edge settings ($\alpha = 8.52\%$, $H_{RVE} = 50$ mm).

Cell size (mm)	2.5 ~ 2.7	2.8 ~ 3.1	3.2 ~ 3.5	3.6 ~ 4.1	4.2 ~ 4.9	5.0 ~ 5.5
n_{edge}	40	36	32	28	24	20
h_{edge} (mm)	0.6918	0.8723	1.1333	1.2592	1.5188	2.0196

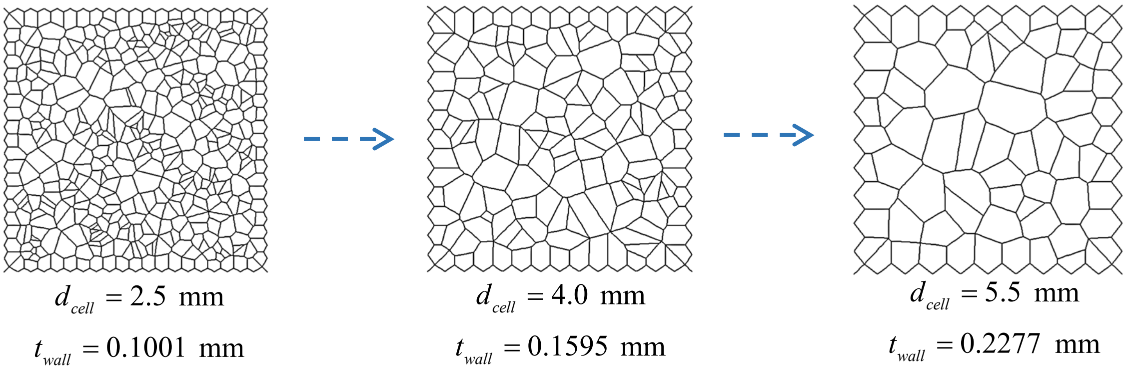

Fig. 6. RVE cases under the same relative density ($\alpha = 8.52\%$, $H_{RVE} = 50$ mm).

Figs. 7A and 7B plot the average cell wall thickness versus cell size and average total cell wall length versus cell number curves, respectively. It is found that the cell wall thickness increases almost linearly when the cell size rises. Meanwhile, the cell number changes from 466 to 96, leading to a monotonic drop of cell wall length. The coefficients of variation shown in both figures are below 1.5%, verifying the representativeness of mean values averaged from five porosity configuration cases. Note that the estimated cell wall thicknesses are achievable for Aluminium foams [46]. In addition, it appears that a smaller cell size leads to more stable results, according to the general trends of coefficient of variation.

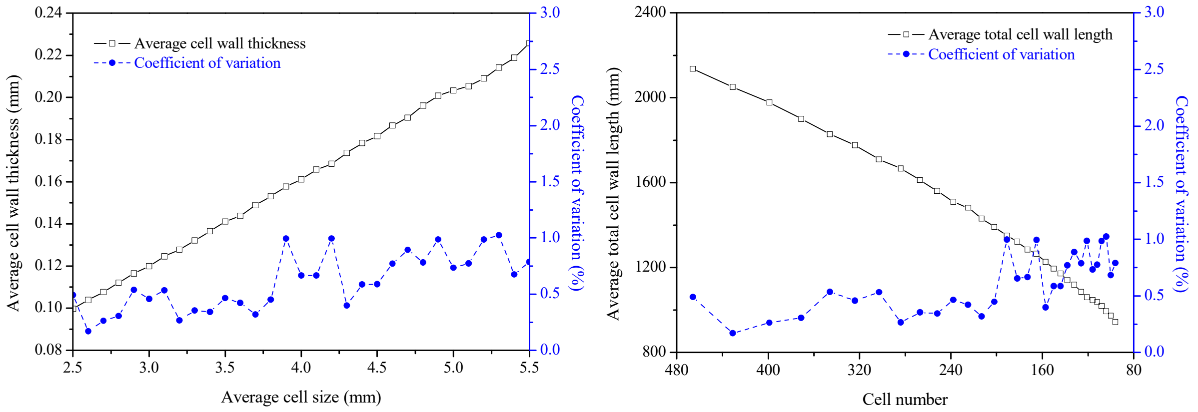

(A) Cell wall thickness (B) Total cell wall length

Fig. 7. Cell wall thicknesses and total cell wall lengths of RVEs under the same relative density ($\alpha = 8.52\%$, $H_{RVE} = 50$ mm, each data point is averaged from five cases).

The corresponding data points of obtained RVE Young's modulus are illustrated in Fig. 8A with respect of the average cell size. A range of 993.46 ~ 1136.29 MPa can be observed (average value: 1063.71 MPa), where the related porosity configurations for maximum and minimum values are also disclosed. The related elementary strain energy distributions are given under 1% vertical compression (Loading scenario I, element solution, SENE), indicating that the cell wall deformations are more evenly distributed for the RVE model with a higher Young's modulus, while for its counterpart with a smaller modulus, deformations are rather localised on the cell walls of larger internal pores. Fig. 8B highlights that the RVE Young's modulus (averaged from the data in Fig. 8A) remains nearly unchanged under the same relative density, regardless of the varying cell sizes and cell wall thicknesses. This finding is aligned with the conclusion of existing studies about metal foams [47]. Moreover, the corresponding coefficient of variation peaks at 2.72% when $d_{cell} = 3.5$ mm. With the material consumption of 8.52%, Aluminium foams can achieve 1.724% (=1063.71/61700) of the Young's modulus of base materials under the same external volume.

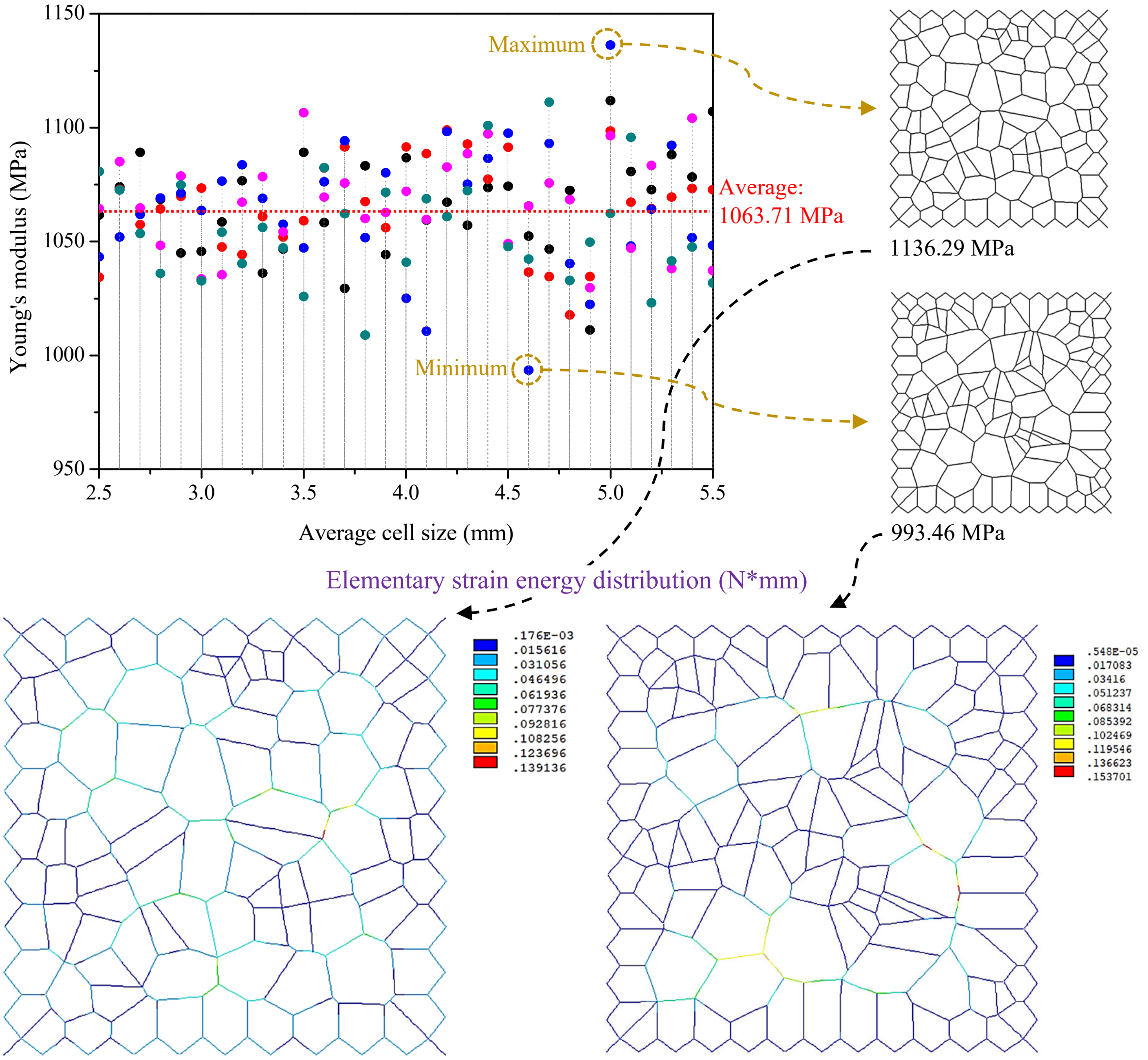

(A) Young's modulus data points and elementary strain energy distributions

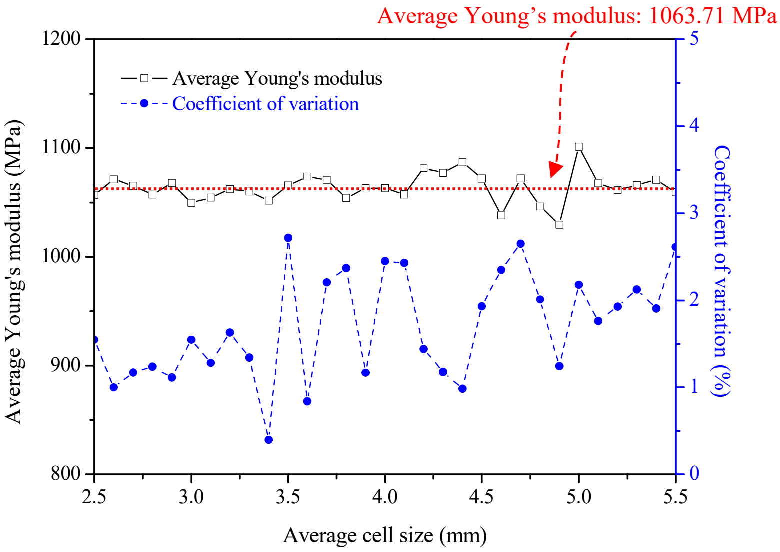

(B) Young's modulus (averaged from data in (A)) versus cell size

Fig. 8. RVE Young's moduli under the same relative density ($\alpha = 8.52\%$, $H_{RVE} = 50$ mm).

2.3.4. Varying relative densities

We then look at the effect of relative density. Due to the slenderness ratio requirement of Timoshenko beam element in FE simulations, the proposed RVE models are only applicable to high-porosity foams with low relative densities, leading to a target range of $\alpha = 4\% \sim 13\%$ in this study. Five porosity configurations are used for each calculation case with designated relative density and cell size, resulting in the changes of averaged cell wall thickness, Young's modulus, and coefficient of variation for discussion. A total of 470 RVEs are assessed in this section with the edge settings in Table 7.

Firstly, RVEs with cell sizes fixed at 4.0, 4.5, and 5.0 mm are generated, where the increasing cell wall thickness raises the relative density (see Fig. 9A). While their Young's modulus versus relative density curves follow a trend of overlapping (see Fig 9B), confirming the conclusion from section 2.3.3, i.e., the relative density is the determining factor when evaluating the foam's Young's modulus. Furthermore, there is no obvious change in the average total cell wall length (not listed here) because the cell number remains close when the cell size is constant, despite of a varying relative density over a small range ($5\% \sim 10\%$).

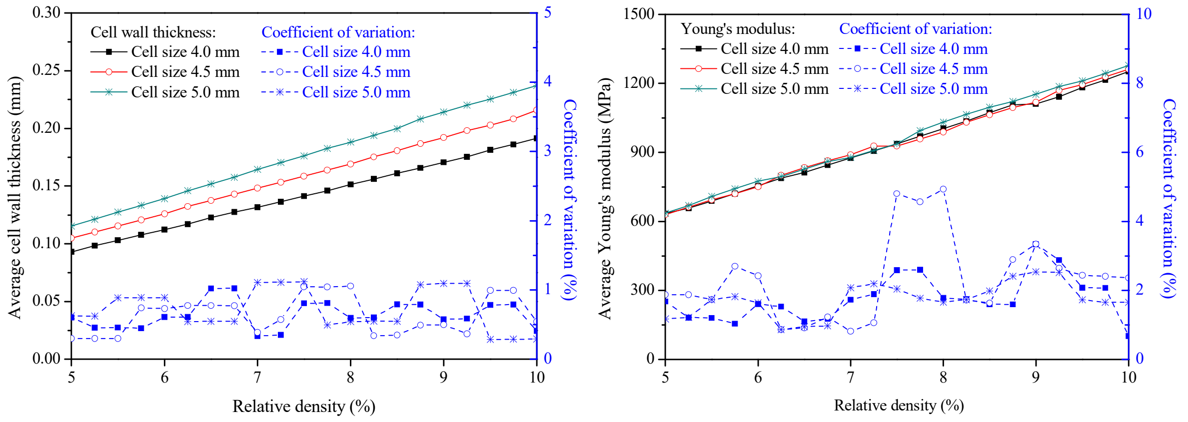

(A) Cell wall thickness (B) Young's modulus

Fig. 9. Results of RVEs with fixed cell sizes under varying relative densities ($H_{RVE} = 50$ mm, each data point is averaged from five cases).

Secondly, the average cell size and cell wall thickness are adjusted simultaneously to achieve a wide range of relative density: $4\% \sim 13\%$. It is clear that the variation curve of the cell wall thickness in Fig. 10A is nonlinear, and the corresponding total cell wall length in Fig. 10B changes monotonically with respect to the cell number. The largest value of the average cell wall thickness (0.1677 mm) is adopted in the RVE model with the cell size and relative density as 3.4 mm and 10.3%, respectively. The corresponding RVE Young's moduli are shown in Fig. 10C and rise evidently under a higher relative density.

In terms of the coefficient of variation, those for cell wall thickness and total cell wall length are lower than 1.5% (see Figs. 9A, 10A, and 10B), while the fluctuation of Young's modulus is more obvious (see Figs. 9B and 10C) with the maximum coefficient value reaching 4.93% when the cell size equals to 4.5 mm and the relative density is 8.0% (see Fig. 9B).

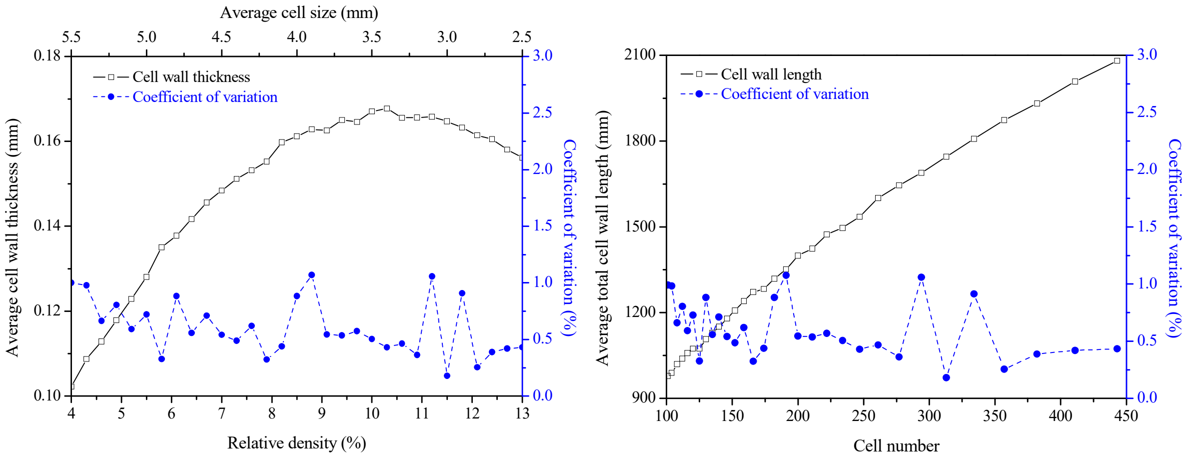

(A) Cell wall thickness (B) Total cell wall length

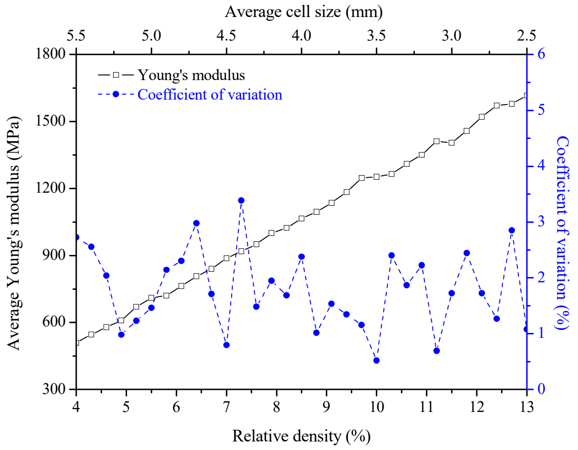

(C) Young’s modulus

Fig. 10. Results of RVEs with changing cell sizes under varying relative densities ($H_{RVE} = 50$ mm, each data point is averaged from five cases).

2.4. Data fitting

Based on the RVE results from section 2.3, we employ the curve-fitting technique (MATLAB routine lsqcurvefit) with a nonlinear least-squares solver to develop empirical equations for the prediction of foam Young’s moduli (Figs 9B and 10C) and RVE cell wall lengths (Figs. 7B and 10B). As evidenced by Fig. 11, the change in the Young’s modulus ratio E^* / E_s against relative density α well satisfies

$$\frac{E^*}{E_s} = 0.2032\alpha \tag{6}$$

in which E^* is the foam modulus and E_s denotes that of base materials. The coefficient of determination R^2 evaluates the goodness of fit of Eq. (6):

$$R^2 = 1 - \frac{\sum_i (y_i - p_i)^2}{\sum_i (y_i - \bar{y})^2} \tag{7}$$

where y_i is the result from RVE simulation, p_i indicates the predicted one via Eq. (6), and $\bar{y}$ is the mean of y_i. In case of multiple data points with the same horizontal coordinate, y_i represents their average value. The obtained R^2 ($= 0.99837$) suggests a close correlation between the original and predicted datasets.

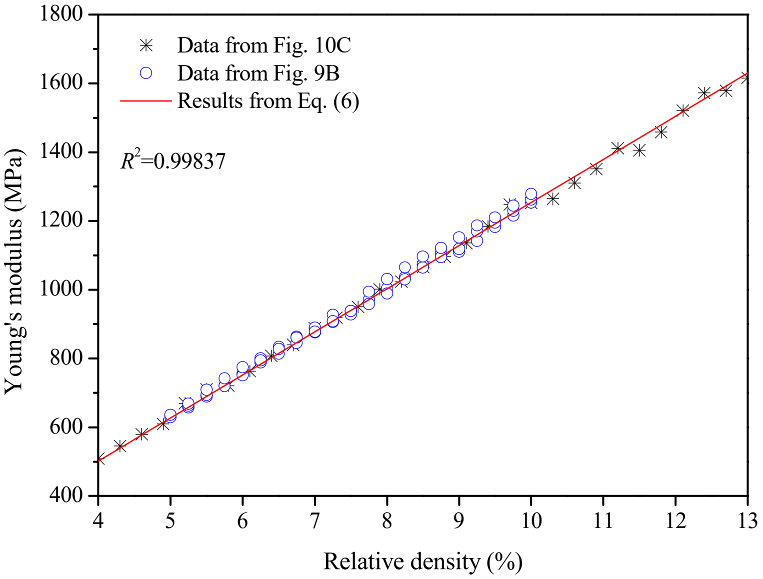

Fig. 11. Data fitting on RVE Young's modulus.

Similar equations have been proposed by existing studies to estimate the quantitative relationship between foam Young's modulus and relative density:

$$\frac{E^*}{E_s} = 0.3163\alpha \tag{8}$$

$$\frac{E^*}{E_s} = 0.3188\alpha^2 + 0.3163\alpha \tag{9}$$

$$\frac{E^*}{E_s} = 0.5625\alpha^2 + 0.25\alpha \tag{10}$$

$$\frac{E^*}{E_s} = \left(0.1 \sim 1.0\right)\left(0.5\alpha^2 + 0.3\alpha\right) \tag{11}$$

$$\frac{E^*}{E_s} = \alpha^{1.72} \text{ (simplified from } \frac{E^*}{E_s} = \alpha^{1.72\pm 0.10} \text{ in [48])} \tag{12}$$

where Eq. (8) predicts the upper bound elastic moduli of high-porosity closed-cell foams ($\alpha < 20\%$) [49], Eq. (9) also applies for foams with $\alpha < 20\%$ and is established based on FE simulations of regular closed-cell tetrakaidecahedral foams by using continuum elements [38, 50], Eq. (10) is set up for comparison purposes and derived using idealized cubic cell model [38, 51], Eq. (11) indicates a well-accepted way to measure the Young's modulus range of closed-cell metal foams [47], and Eq. (12) is constructed from the power-law model fitting of experimental results ($16\% \le \alpha \le 100\%$) [48].

A direct comparison among predictions from Eq. (6) and the existing ones (Eqs. (8)-(12)) is depicted in Fig. 12, where results in validation case A [42] and other experiments with ALPORAS closed-cell Aluminium foams [38] are also enclosed. The data of bottom and middle specimen regions in [38] are presented. It is observed that most of the obtained Young's modulus ratios are within the range of the predicted upper bound (Eqs. (8) and (11)) and lower bound (Eq. (11)). Those from Eqs. (9)-(10) are close to the upper bound and significantly overestimate compared to the test results, aligning with the findings reported in [51, 52]. The ratios from Eq. (6) and Eq. (12) match reasonably well. The gap between predicted and experimental results may be explained by the imperfections in the test specimens, such as broken cell walls [38] and cell wall curves and wriggles [49], leading to a drop in Young's modulus.

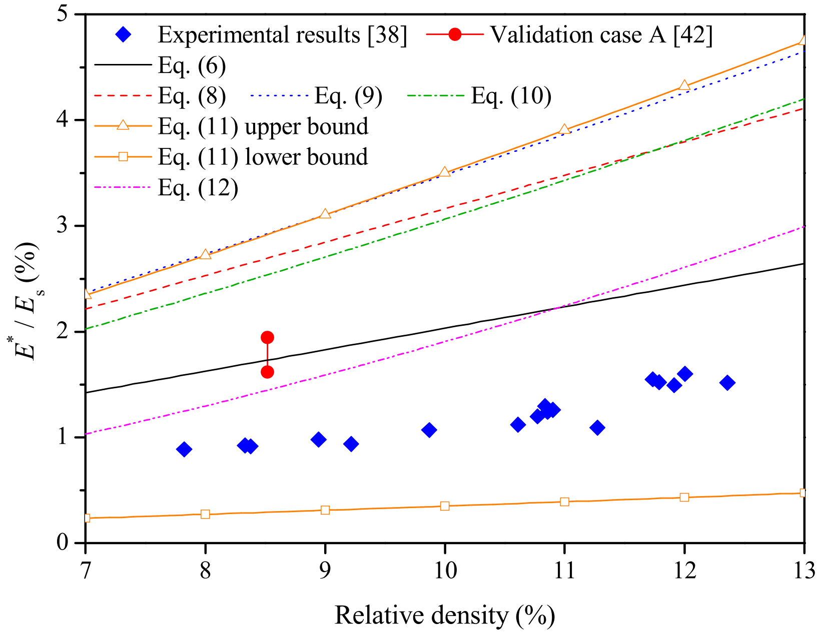

Fig. 12. Predictions on Young's modulus of closed-cell Aluminium foams.

It is worthwhile noting that the total cell wall length can be linked to cell number quantitatively via data fitting (see Fig. 13, $R^2 = 0.99900$):

$$\frac{L_{wall}}{H_{RVE}} = 1.966\sqrt{N_{RVE}} \tag{13}$$

leading to

$$\alpha = \frac{-A^2 + A\sqrt{A^2 + 4\pi}}{2\pi} \tag{14}$$

of which $A = 3.932\left(t_{wall} / d_{cell}\right)$. Therefore,

$$\frac{E^*}{E_s} = 0.2032\left(\frac{-A^2 + A\sqrt{A^2 + 4\pi}}{2\pi}\right) \tag{15}$$

Eq. (15) is able to well estimate the Young's modulus of closed-cell Aluminium foams according to the cell wall thickness, averaged cell size, and base material properties, as shown in Fig. 14 where $R^2 = 0.99793$. Note that the developed Eqs. (6) and (15) are only applicable to high-porosity low-density closed-cell Aluminium foams due to the aforementioned beam element size restriction in the RVE simulation and the requirement of polyhedral cells.

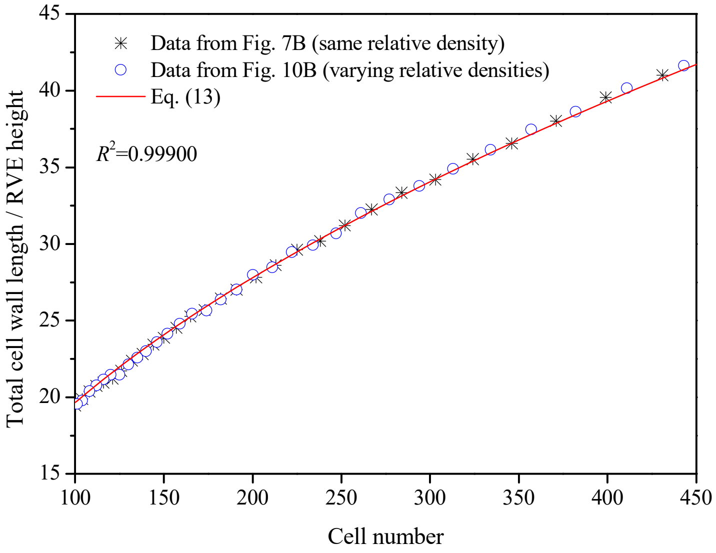

Fig. 13. Data fitting on RVE total cell wall length.

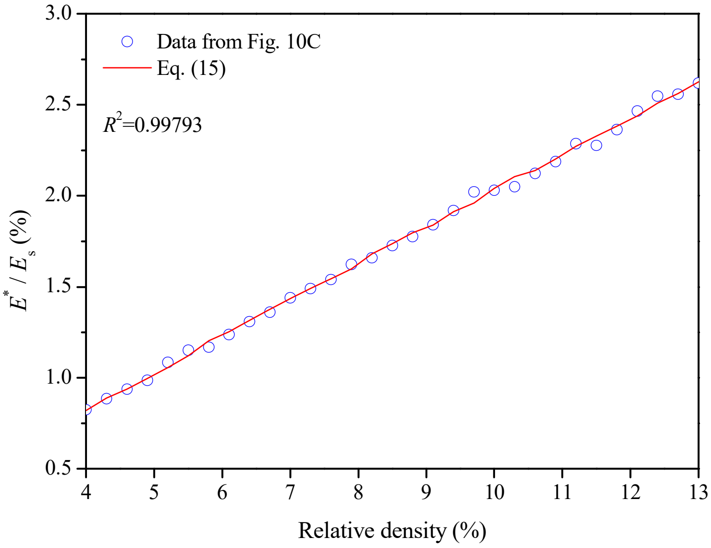

Fig. 14. Predictions on Young's modulus of closed-cell Aluminium foams.

3. Beam buckling and vibration assessments

As mentioned, section 2 connects the mesoscopic porosity features of cellular geometries with the foam's Young's modulus (Eqs. (6) and (15)), while section 3 further links the porosity features to the beam structural performances by using this Young's modulus in the buckling and vibration analyses. Specifically, section 3 proposes a laminated porous beam model (section 3.1), where Eq. (6) gives the beam Young's modulus according to the graded relative density along the thickness direction. The beam formulations are presented afterwards (section 3.2), as well as the corresponding convergence and validation analyses (section 3.3). Finally, the effect of porosity gradation on the beam buckling loads and natural frequencies is elaborated (section 3.4), and this gradation is based on the changing relative density but can be converted into the variations of cell size and cell wall thickness via Eq. (14). Therefore, the connection between porosity features and overall structural behaviours of FG porous beams is established.

3.1. Laminated beam model

A six-layer laminated beam model (length *L*, height H_b, width *b*) made of Aluminium foams under current consideration is described in Fig. 15, where a Cartesian coordinate system (*x*, *z*) is established with *x*-axis ($0 \le x \le L$) along the mid-plane direction and *z*-axis ($-H_b / 2 \le z \le H_b / 2$) across the thickness while pointing downwards. All the layers share the equivalent thickness $\Delta h = H_b / 6$, as well as the same beam width *b*, and are assumed to be perfectly bonded together without regard to delamination. The top and bottom surface layers are named as high-density layers, while those adjacent to the mid-plane are low-density layers, leaving the rest as medium-density layers. The relative densities of different layers change according to

$$\alpha = \begin{cases} 0.085 + 0.045\phi & \text{High-density layer} \\ 0.085 & \text{Medium-density layer} \\ 0.085 - 0.045\phi & \text{Low-density layer} \end{cases} \tag{16}$$

where ϕ ($0 \le \phi \le 1$) indicates a varying porosity distribution. When $\phi = 0$, it suggests a homogeneous beam with uniform porosities ($\alpha = 8.5\%$ for all layers). While in case of $\phi = 1$ (see Fig. 15 for graded porosity examples), the relative density of high-density layers peaks at 13.0% while that of low-density layers is reduced to a minimum value of 4.0%. In this study, the relative density is taken as the principal parameter to determine the elastic properties of beam layers, instead of the average cell size and cell wall thickness, both of which can be further derived according to Eq. (15). The Young's modulus, shear modulus, Poisson ratio, and mass density are represented by $E_{\mathrm{H}}^{*}(\phi)$, $G_{\mathrm{H}}^{*}(\phi)$, $v_{\mathrm{H}}^{*}(\phi)$, $\rho_{\mathrm{H}}^{*}(\phi)$ for high-density layers, E_{M}^{*}, G_{M}^{*}, v_{M}^{*}, ρ_{M}^{*} for medium-density layers, and $E_{L}^{*}(\phi)$, $G_{L}^{*}(\phi)$, $v_{L}^{*}(\phi)$, $\rho_{L}^{*}(\phi)$ for low-density layers. The total mass of this laminated beam remains constant for the purpose of comparison.

Young's modulus ($E_{\mathrm{H}}^{*}(\phi)$, E_{M}^{*}, $E_{L}^{*}(\phi)$) can be computed by using Eq. (6), but the shear modulus and Poisson's ratio of closed-cell foams cannot be properly evaluated with the proposed RVE models due to the restriction of a 2D analysis. Therefore, we adopt existing equations to address this issue: $G_{\mathrm{H}}^{*}(\phi)$, G_{M}^{*}, $G_{L}^{*}(\phi)$ are obtained via [52, 53]

$$\frac{G_{H/M/L}^{*}}{G_s} = \frac{3}{4}\vartheta\left(1+v_s\right)\left(0.5\alpha^2 + 0.3\alpha\right) \tag{17}$$

in which G_s is the shear modulus of base materials, $\vartheta = 0.4886$ backed by validation case A: the foam's shear modulus reaches 330 MPa when $G_s = 23.731$ GPa, $v_s = 0.3$, $\alpha = 8.52\%$ [42]. And $v_{\mathrm{H}}^{*}(\phi)$, v_{M}^{*}, $v_{L}^{*}(\phi)$ can be predicted with [48, 54]

$$v^*_{H/M/L} = v_s + \frac{3(1-5v_s)(1-v_s^2)}{2(7-5v_s)}(1-\alpha) \tag{18}$$

where v_s denotes Poisson's ratio of base materials. Similarly, $\rho^*_{\mathrm{H}}(\phi)$, ρ^*_{M}, $\rho^*_L(\phi)$ are also determined by the base material mass density ρ_s via $\rho^*_{H/M/L} = \alpha\rho_s$. Note that the developed laminated beam model is also linked to Aluminium foam products with specific average cell sizes and cell wall thicknesses, and the porosity examples in Fig. 15 are directly abstracted from RVE models.

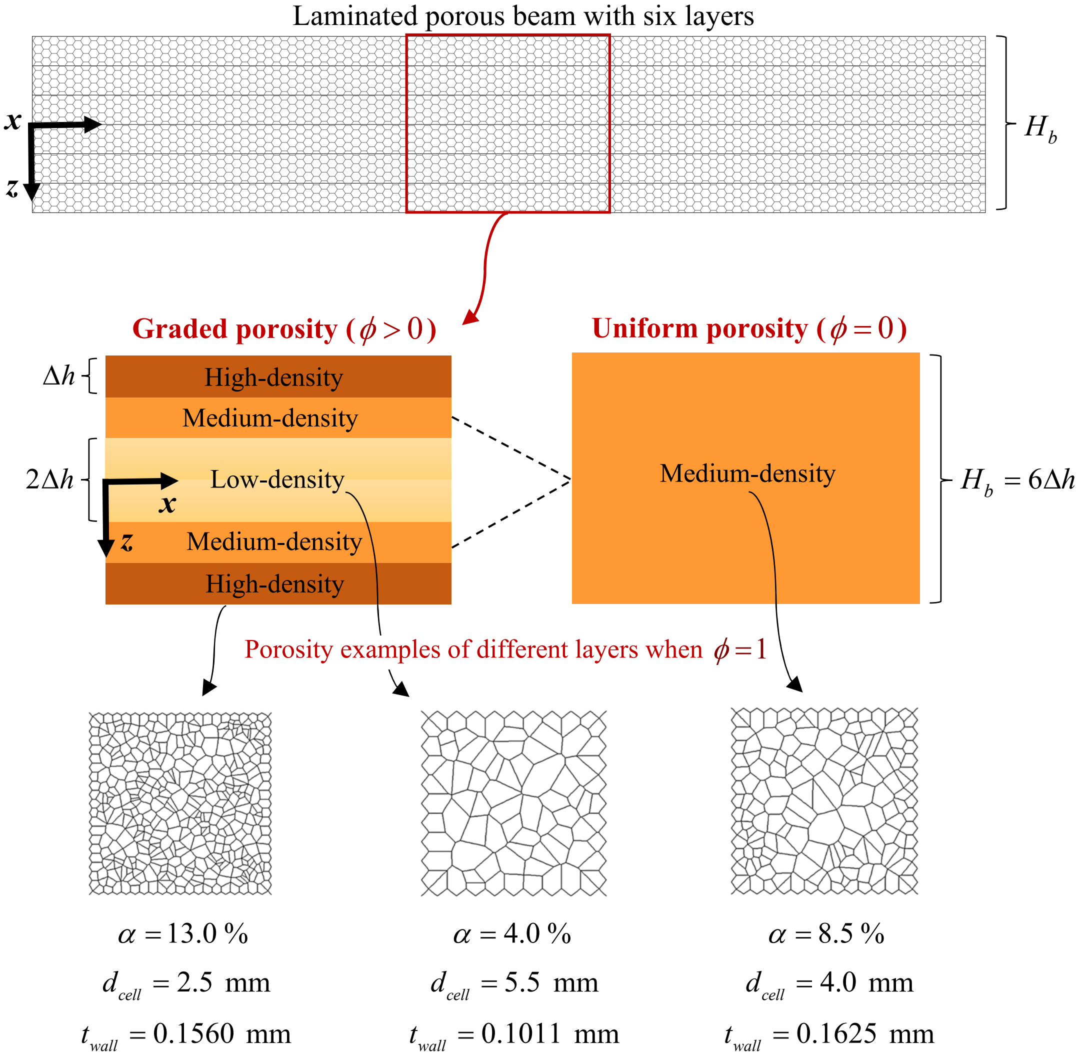

Fig. 15. Illustrations of the laminated porous beam model and graded porosities.

3.2. Formulations of beam analysis

The displacement field of shear deformable laminated beams [55] is constructed by Timoshenko beam theory as

$$\begin{cases} u(x,z,t) = u_0(x,t) + z\varphi_0(x,t) \\ w(x,z,t) = w_0(x,t) \end{cases} \tag{19}$$

where u and w represent the displacements along x- and z-axes, while u_0 and w_0 are those on the mid-plane, φ_0 denotes the cross-section rotation, and t is time. We adopt the following strain-displacement relationship

$$\begin{cases} \varepsilon_{xx} = \left(\partial u_0 / \partial x\right) + z\left(\partial \varphi_0 / \partial x\right) \\ \gamma_{xz} = \left(\partial w_0 / \partial x\right) + \varphi_0 \end{cases} \tag{20}$$

of which the normal and transverse shear strains (ε_{xx} and γ_{xz}) are used to calculate the corresponding stress components via

$$\begin{cases} \sigma_{xx} = \dfrac{E^*(z)}{1 - v^*\left(z\right)^2}\varepsilon_{xx} \\ \sigma_{xz} = G^*(z)\gamma_{xz} \end{cases} \tag{21}$$

The strain energy of the porous beam [56] then can be expressed as

$$\begin{aligned} \Psi &= \frac{b}{2}\int_0^L \int_{-H_b/2}^{H_b/2} (\sigma_{xx}\varepsilon_{xx} + \sigma_{xz}\gamma_{xz})\mathrm{d}z\mathrm{d}x \\ &= \frac{b}{2}\int_0^L \left[A_{11}\left(\frac{\partial u_0}{\partial x}\right)^2 + 2B_{11}\frac{\partial \varphi_0}{\partial x}\frac{\partial u_0}{\partial x} + D_{11}\left(\frac{\partial \varphi_0}{\partial x}\right)^2 + A_{55}\left(\varphi_0 + \frac{\partial w_0}{\partial x}\right)^2 \right]\mathrm{d}x \end{aligned} \tag{22}$$

in which the extensional A_{11}, coupling B_{11}, bending D_{11}, and shear A_{55} rigidities are given by

$$\begin{cases} A_{11} = \dfrac{H_b}{3}\dfrac{E_{\mathrm{H}}^{*}(\phi)}{1-v_{\mathrm{H}}^{*}(\phi)^{2}} + \dfrac{H_b}{3}\dfrac{E_{\mathrm{M}}^{*}}{1-v_{\mathrm{M}}^{*2}} + \dfrac{H_b}{3}\dfrac{E_{L}^{*}(\phi)}{1-v_{L}^{*}(\phi)^{2}} \\ B_{11} = 0 \\ D_{11} = \dfrac{19H_b^3}{324}\dfrac{E_{\mathrm{H}}^{*}(\phi)}{1-v_{\mathrm{H}}^{*}(\phi)^{2}} + \dfrac{7H_b^3}{324}\dfrac{E_{\mathrm{M}}}{1-v_{\mathrm{M}}^{2}} + \dfrac{H_b^3}{324}\dfrac{E_{L}^{*}(\phi)}{1-v_{L}^{*}(\phi)^{2}} \\ A_{55} = \dfrac{1}{3}kH_b\left[G_{\mathrm{H}}^{*}(\phi) + G_{\mathrm{M}}^{*} + G_{L}^{*}(\phi)\right] \end{cases} \tag{23}$$

where $k = 5/6$ is the shear correction factor. The work done by the axial force N_x along the beam length is written as

$$V = \int_0^L \left[\frac{1}{2}N_x\left(\frac{\partial w_0}{\partial x}\right)^2\right]\mathrm{d}x \tag{24}$$

and the beam kinetic energy reads

$$T = \frac{b}{2}\int_0^L \left[I_0\left(\frac{\partial u_0}{\partial t}\right)^2 + 2I_1\frac{\partial u_0}{\partial t}\frac{\partial \varphi_0}{\partial t} + I_2\left(\frac{\partial \varphi_0}{\partial t}\right)^2 + I_0\left(\frac{\partial w_0}{\partial t}\right)^2\right]\mathrm{d}x \tag{25}$$

of which the inertia items are computed by

$$\begin{cases} I_0 = \dfrac{H_b}{3}\left[\rho_{\mathrm{H}}^{*}(\phi) + \rho_{\mathrm{M}}^{*} + \rho_{L}^{*}(\phi)\right] \\ I_1 = 0 \\ I_2 = \dfrac{19H_b^3}{324}\rho_{\mathrm{H}}^{*}(\phi) + \dfrac{7H_b^3}{324}\rho_{\mathrm{M}}^{*} + \dfrac{H_b^3}{324}\rho_{L}^{*}(\phi) \end{cases} \tag{26}$$

Therefore, the total energy functional of this system can be obtained as

$$\begin{cases} \Pi_1 = \Psi - V & \text{Buckling analysis} \\ \Pi_2 = \Psi + T & \text{Vibration analysis} \end{cases} \tag{27}$$

The Ritz method is employed to solve the governing equations with the following trial functions for hinged-hinged (H-H), clamped-clamped (C-C), clamped-hinged (C-H), and clamped-free (C-F) end supports [57]:

H-H beam:

$$\begin{cases} u_0 / H_b = \sum_{j=1}^{N} \zeta_{1j} \left(x/L \right)^j (1 - x/L) \\ w_0 / H_b = \sum_{j=1}^{N} \zeta_{2j} \left(x/L \right)^j (1 - x/L) \\ \varphi_0 = \sum_{j=1}^{N} \zeta_{3j} \left(x/L \right)^{j-1} \end{cases} \quad (28)$$

C-C beam:

$$\begin{cases} u_0 / H_b = \sum_{j=1}^{N} \zeta_{1j} \left(x/L \right)^j (1 - x/L) \\ w_0 / H_b = \sum_{j=1}^{N} \zeta_{2j} \left(x/L \right)^j (1 - x/L) \\ \varphi_0 = \sum_{j=1}^{N} \zeta_{3j} \left(x/L \right)^j (1 - x/L) \end{cases} \quad (29)$$

C-H beam:

$$\begin{cases} u_0 / H_b = \sum_{j=1}^{N} \zeta_{1j} \left(x/L \right)^j (1 - x/L) \\ w_0 / H_b = \sum_{j=1}^{N} \zeta_{2j} \left(x/L \right)^j (1 - x/L) \\ \varphi_0 = \sum_{j=1}^{N} \zeta_{3j} \left(x/L \right)^j \end{cases} \quad (30)$$

C-F beam:

$$\begin{cases} u_0 / H_b = \sum_{j=1}^{N} \zeta_{1j} \left(x/L \right)^j \\ w_0 / H_b = \sum_{j=1}^{N} \zeta_{2j} \left(x/L \right)^j \\ \varphi_0 = \sum_{j=1}^{N} \zeta_{3j} \left(x/L \right)^j \end{cases} \quad (31)$$

where N is the total number of polynomial terms. The standard procedure of Ritz method leads to

$$\frac{\partial \Pi^*}{\partial \zeta_{1j}} = 0, \ \frac{\partial \Pi^*}{\partial \zeta_{2j}} = 0, \ \frac{\partial \Pi^*}{\partial \zeta_{3j}} = 0 \quad (32)$$

in which Π^* is the dimensionless energy form ($\frac{\Pi_1}{A_{110} H_b^2 b / L}$ or $\frac{\Pi_2}{A_{110} H_b^2 b / L}$), and $A_{110} = \frac{E_{\mathrm{M}}^* H_b}{1 - \nu_{\mathrm{M}}^{*2}}$.

And the governing equations are derived as (assuming harmonic oscillations for vibration)

$$\begin{cases} \left(\mathbf{K} - P\mathbf{V} \right) \mathbf{d} = \mathbf{0} & \text{Buckling analysis} \\ \left(\mathbf{K} - \omega^2 \mathbf{M} \right) \mathbf{d} = \mathbf{0} & \text{Vibration analysis} \end{cases} \quad (33)$$

where the unknown coefficient vector $\mathbf{d} = \{ \{\zeta_{1j}\}^{\mathrm{T}} \{\zeta_{2j}\}^{\mathrm{T}} \{\zeta_{3j}\}^{\mathrm{T}} \}^{\mathrm{T}}$, $j = 1, 2, \ldots, N$, $\mathbf{K}$, $\mathbf{M}$, and $\mathbf{V}$ are the stiffness, mass, and geometric matrices, respectively. The dimensionless buckling load $P_{cr} = \frac{N_x}{A_{110} b}$ and fundamental natural frequency $\omega = \Omega L \sqrt{\frac{I_{10}}{A_{110}}}$ (Ω is the angular natural frequency and $I_{10} = \rho_{\mathrm{M}}^{*} H_b$) are the lowest eigenvalues of Eq. (33).

3.3. Convergence and Validation

In sections 3.3 and 3.4, the base material properties of closed-cell aluminium foams in Table 1 are utilised to compute the dimensionless critical buckling load P_{cr} and fundamental natural frequency ω, which are presented in most occasions except for Table 9 where non-dimensionless results are listed to be compared with the outcomes from other methods. A convergence analysis is first carried out, as given in Table 8. It is obvious that both buckling load and natural frequency converge under a larger number of polynomial terms in the trial functions, and $N = 10$ are adopted in the subsequent calculations.

Table 8

Convergence analysis of FG porous beams ($\phi = 1$, $L / H_b = 20$).

Boundary conditions	$N = 4$	$N = 6$	$N = 8$	$N = 10$	$N = 12$
	Dimensionless critical buckling load				
H-H	2.76E-03	2.76E-03	2.76E-03	2.76E-03	2.76E-03
C-H	5.59E-03	5.56E-03	5.56E-03	5.56E-03	5.56E-03
C-C	1.12E-02	1.07E-02	1.07E-02	1.07E-02	1.07E-02
C-F	6.95E-04	6.95E-04	6.95E-04	6.95E-04	6.95E-04
	Dimensionless fundamental natural frequency				
H-H	0.1648	0.1647	0.1647	0.1647	0.1647
C-H	0.2551	0.2548	0.2548	0.2548	0.2548
C-C	0.3663	0.3654	0.3654	0.3654	0.3654
C-F	0.0589	0.0589	0.0589	0.0589	0.0589

In order to verify the formulations in section 3.2, the present results are compared with the counterparts obtained from full-scale FE models in ANSYS/Workbench (version: 2020 R2, SOLID187 elements, elastic moduli referred to Eq. (21), $H_b = b = 0.1$ m) and the following theoretical equations for homogeneous beams:

Euler's critical load (N):

$$P_T = \frac{\pi^2 E_T I_T}{(\lambda L)^2} \tag{34}$$

Regular fundamental natural frequency (Hz):

$$\Omega_{H-H} = \frac{\pi}{2L^2}\sqrt{\frac{E_T I_T}{\rho_T b H_b}} \text{ for H-H beam [58]} \tag{35}$$

$$\Omega_{C-F} = \frac{(1.875)^2}{2\pi L^2}\sqrt{\frac{E_T I_T}{\rho_T b H_b}} \text{ for C-F beam [59]} \tag{36}$$

where $E_T = E_{\mathrm{M}}^* / \left(1 - v_{\mathrm{M}}^{*2}\right)$, $I_T = bH_b^3/12$, $\rho_T = \rho_M^*$, $\lambda = 1, 0.7, 0.5, 2$ correspond to H-H, C-H, C-C, and C-F beams, respectively. As can be observed in Table 9, a good agreement is reached across the outcomes from different analysis approaches for porous beams with various porosity distributions and end supports, highlighting the validity of the present formulations.

Table 9
Validation analysis of porous beams ($L/H_b = 20$).

	H-H	**C-H**	**C-C**	**C-F**
	Critical buckling load (N, $\phi = 1$, FG beam)			
Present	30433	61426	117896	7671
ANSYS	31345	62905	120510	7954
	Regular fundamental natural frequency (Hz, $\phi = 1$, FG beam)			
Present	28.75	44.48	63.78	10.28
ANSYS	29.17	44.89	63.98	10.46
	Critical buckling load (N, $\phi = 0$, homogeneous beam)			
Present	22515	45593	87896	5664
ANSYS	23364	47429	91788	5855
Theoretical (Eq. (34))	22701	46330	90806	5675
	Regular fundamental natural frequency (Hz, $\phi = 0$, homogeneous beams)			
Present	24.74	38.36	55.16	8.84
ANSYS	25.17	39.05	56.16	9.00
Theoretical (Eqs. (35)-(36))	24.86			8.86

3.4. Parametric studies on FG porous beams

In what follows, the structural performance of FG porous beams is assessed with a focus on the influence of porosity distribution. Fig. 16 illustrates the effects of ϕ on the dimensionless critical buckling load and fundamental natural frequency under different beam boundary conditions. It is found that an evident improvement on the buckling and vibration resistance is achieved with an increase in ϕ. The improvements of C-F beams can reach 35.4% for the buckling load and 16.3% for the natural frequency when $L/H_b = 20$, suggesting a stiffer beam consisting of graded porosities. Moreover, the discrepant results originated from different end supports indicate that beams are more stable in a fully clamped condition. Here ϕ determines the variation of relative density and can be further translated into average cell size and cell wall thickness distributions via Eq. (14).

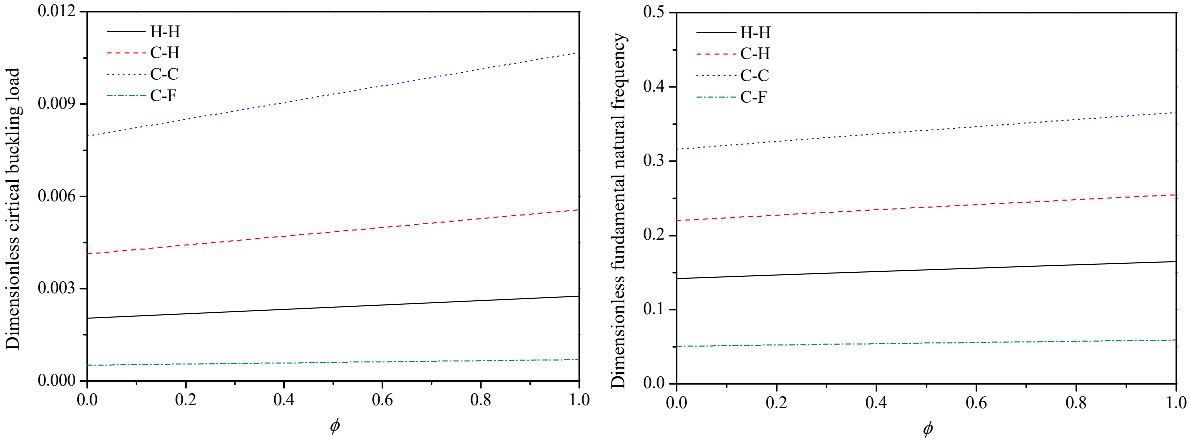

(A) Critical buckling load (B) Fundamental natural frequency

Fig. 16. Effects of ϕ on the dimensionless critical buckling loads and fundamental natural frequencies of FG porous beams ($L/H_b = 20$).

Tables 10 and 11 tabulate the dimensionless critical buckling loads and fundamental natural frequencies of beams with a changing porosity distribution (ϕ) and slenderness ratio (L/H_b). Our data confirm that beams with better structural stability and higher vibration resistance are made of non-uniform porosities, especially in case of $\phi = 1$. When comparing

FG beams ($\phi = 1$) and their homogeneous counterparts ($\phi = 0$), changes in P_{cr} and ω are minimised at 30.6% and 13.7% for the C-C beam with $L / H_b = 10$, while peak at 35.5% and 16.4% for the C-F beam with $L / H_b = 30$. Generally, significant improvements of over 30% and 10% for buckling loads and natural frequencies are observed, respectively.

Table 10
Dimensionless critical buckling loads of FG porous beams.

ϕ	**H-H**	**C-H**	**C-C**	**C-F**
		$L / H_b = 10$		
0	7.96E-03	1.57E-02	2.91E-02	2.04E-03
0.5	9.32E-03	1.82E-02	3.35E-02	2.40E-03
1	1.07E-02	2.08E-02	3.79E-02	2.76E-03
		$L / H_b = 20$		
0	2.04E-03	4.13E-03	7.96E-03	5.13E-04
0.5	2.40E-03	4.85E-03	9.32E-03	6.04E-04
1	2.76E-03	5.56E-03	1.07E-02	6.95E-04
		$L / H_b = 30$		
0	9.11E-04	1.85E-03	3.60E-03	2.28E-04
0.5	1.07E-03	2.18E-03	4.23E-03	2.69E-04
1	1.23E-03	2.51E-03	4.86E-03	3.09E-04

Table 11
Dimensionless fundamental natural frequencies of FG porous beams.

ϕ	**H-H**	**C-H**	**C-C**	**C-F**
		$L / H_b = 10$		
0	0.2792	0.4243	0.5957	0.1005
0.5	0.3020	0.4568	0.6384	0.1089
1	0.3230	0.4867	0.6774	0.1167
		$L / H_b = 20$		
0	0.1417	0.2198	0.3161	0.0506
0.5	0.1537	0.2380	0.3417	0.0549
1	0.1647	0.2548	0.3654	0.0589
		$L / H_b = 30$		
0	0.0948	0.1475	0.2132	0.0338
0.5	0.1028	0.1599	0.2310	0.0367
1	0.1102	0.1714	0.2474	0.0393

4. Conclusions

This paper employs the multiscale modelling techniques by proposing RVE models to evaluate the relation between Young's modulus and meso-structures of closed-cell foams, followed by a mechanical assessment of laminated FG porous beams to provide practical advice on the design of porous structural components with promoted buckling and vibration performances. The key findings from this study are:

(1) The proposed RVE model is able to predict the Young's modulus of closed-cell foams with specified relative densities, average cell sizes, and base material properties.

(2) According to the parametric study based on Aluminium foams (validation case A), the RVE external size, loading scenario, average cell size, cell wall thickness, and randomised porosity configuration do not evidently influence the obtained Young's modulus under the same relative density which is demonstrated as the determining factor for foam stiffness.

(3) Eqs. (6) and (15) are constructed via data fitting and directly connect the Young's modulus with the porosity features of closed-cell Aluminium foams.

(4) The examination of laminated FG beams indicates that graded porosity distributions with an increase in ϕ enhance the beam stiffness, leading to larger critical buckling loads and higher fundamental natural frequencies, of which the improvements reach over 30% and 10% for the discussed beams, respectively. The vibration of ϕ is related to the changes in the relative density, average cell size, and cell wall thickness.

(5) The adopted multiscale modelling framework, by combining FE homogenisation and structural assessment, offers important insights into the design of porous structures, and discloses the quantitative relationship between mesoscopic porosity features and overall mechanical behaviours.

Although the adopted FE homogenisation provides a relatively sound basis for the structural analysis of metal foam components, our research can be further improved by considering various imperfections in the FE model (such as curving and broken cell walls), as well as the variation in the cell wall thickness and the possible influence of air enclosed by cell walls. In addition, extending the current study to a 3D analysis is another way to reach a more accurate prediction.

Acknowledgement

The authors Chen, Schneider, Xu acknowledge the financial support of the ’Future Talent’ Short-term Scholarship of Technical University of Darmstadt. Xu acknowledges the financial support by the German Science Foundation in the framework of the project 460684687. This research was also supported by the Australian Research Council (Chen: ARC DECRA DE220100876).

References

[1] Benedetti M, Du Plessis A, Ritchie R, Dallago M, Razavi S, Berto F. Architected cellular materials: A review on their mechanical properties towards fatigue-tolerant design and fabrication. Materials Science and Engineering: R: Reports 2021;144:100606.

[2] García-Moreno F. Commercial applications of metal foams: Their properties and production. Materials 2016;9:85.

[3] Maconachie T, Leary M, Lozanovski B, Zhang X, Qian M, Faruque O, Brandt M. SLM lattice structures: Properties, performance, applications and challenges. Materials & Design 2019;183:108137.

[4] Smith B, Szyniszewski S, Hajjar J, Schafer B, Arwade S. Steel foam for structures: A review of applications, manufacturing and material properties. Journal of Constructional Steel Research 2012;71:1-10.

[5] Shen J, Lu G, Zhao L, Zhang Q. Short sandwich tubes subjected to internal explosive loading. Engineering Structures 2013;55:56-65.

[6] Wu H, Yang J, Kitipornchai S. Mechanical analysis of functionally graded porous structures: A review. International Journal of Structural Stability and Dynamics 2020;20:2041015.

[7] Magnucki K, Stasiewicz P. Elastic buckling of a porous beam. Journal of Theoretical and Applied Mechanics 2004;42:859-68.

[8] Magnucka-Blandzi E. Dynamic stability of a metal foam circular plate. Journal of Theoretical and Applied Mechanics 2009;47:421-33.

[9] Magnucka-Blandzi E. Axi-symmetrical deflection and buckling of circular porous-cellular plate. Thin-Walled Structures 2008;46:333-7.

[10] Chen D, Yang J, Kitipornchai S. Elastic buckling and static bending of shear deformable functionally graded porous beam. Composite Structures 2015;133:54-61.

[11] Chen D, Yang J, Kitipornchai S. Free and forced vibrations of shear deformable functionally graded porous beams. International Journal of Mechanical Sciences 2016;108:14-22.

[12] Chen D, Kitipornchai S, Yang J. Nonlinear free vibration of shear deformable sandwich beam with a functionally graded porous core. Thin-Walled Structures 2016;107:39-48.

[13] Chen D, Kitipornchai S, Yang J. Postbuckling of shear deformable sandwich beam with a functionally graded porous metal foam core. Proceedings of the 24th Australasian Conference on the Mechanics of Structures and Materials. CRC Press; 2016. p. 1797-1802.

[14] Chen D, Yang J, Kitipornchai S. Buckling and bending analyses of a novel functionally graded porous plate using Chebyshev-Ritz method. Archives of Civil and Mechanical Engineering 2019;19:157-70.

[15] Gao K, Li R, Yang J. Dynamic characteristics of functionally graded porous beams with interval material properties. Engineering Structures 2019;197:109441.

[16] Wu D, Liu A, Huang Y, Huang Y, Pi Y, Gao W. Dynamic analysis of functionally graded porous structures through finite element analysis. Engineering Structures 2018;165:287-301.

[17] Twinkle C, Pitchaimani J. Free vibration and stability of graphene platelet reinforced porous nano-composite cylindrical panel: Influence of grading, porosity and non-uniform edge loads. Engineering Structures 2021;230:111670.

[18] Masjedi PK, Maheri A, Weaver PM. Large deflection of functionally graded porous beams based on a geometrically exact theory with a fully intrinsic formulation. Applied Mathematical Modelling 2019;76:938-57.

[19] Hassani A, Habibolahzadeh A, Bafti H. Production of graded aluminum foams via powder space holder technique. Materials & Design 2012;40:510-5.

[20] Hangai Y, Morita T, Utsunomiya T. Functionally graded aluminum foam consisting of dissimilar aluminum alloys fabricated by sintering and dissolution process. Materials Science and Engineering: A 2017;696:544-51.

[21] Hangai Y, Takahashi K, Utsunomiya T, Kitahara S, Kuwazuru O, Yoshikawa N. Fabrication of functionally graded aluminum foam using aluminum alloy die castings by friction stir processing. Materials Science and Engineering: A 2012;534:716-9.

[22] Iasiello M, Bianco N, Chiu WK, Naso V. Thermal conduction in open-cell metal foams: Anisotropy and Representative Volume Element. International Journal of Thermal Sciences 2019;137:399-409.

[23] Dannemann KA, Lankford Jr J. High strain rate compression of closed-cell aluminium foams. Materials Science and Engineering: A 2000;293:157-64.

[24] Verma KS, Panthi SK, Mondal D. Compressive deformation behavior of closed cell LM-13 aluminum alloy foam using finite element analysis. Materials Today: Proceedings 2020;28:1073-7.

[25] Kurniati EO, Dirgantara T, Gunawan L, Jusuf A. Meso-modeling of Closed-Cell Aluminum Foam Under Compression Loading. Advances in Lightweight Materials and Structures: Springer; 2020. p. 3-17.

[26] Fang Q, Zhang J, Zhang Y, Liu J, Gong Z. Mesoscopic investigation of closed-cell aluminum foams on energy absorption capability under impact. Composite Structures 2015;124:409-20.

[27] Chen D, Kitipornchai S, Yang J. Dynamic response and energy absorption of functionally graded porous structures. Materials & Design 2018;140:473-87.

[28] Zhang J, Zhao G, Lu T. Dynamic responses of sandwich beams with gradient-density aluminum foam cores. International Journal of Protective Structures 2011;2:439-51.

[29] Liang M, Li Z, Lu F, Li X. Theoretical and numerical investigation of blast responses of continuous-density graded cellular materials. Composite Structures 2017;164:170-9.

[30] Schroeder J, Labusch M, Keip M-A. Algorithmic two-scale transition for magneto-electro-mechanically coupled problems: FE2-scheme: Localization and homogenization. Computer methods in applied mechanics and engineering 2016;302:253-80.

[31] Yang Y, Fathidoost M, Oyedeji TD, Bondi P, Zhou X, Egger H, Xu BX. A diffuse-interface model of anisotropic interface thermal conductivity and its application in thermal homogenization of composites. Scripta Materialia 2022;212:114537.

[32] Zhou X, Yang Y, Bharech S, Lin B, Schröder J, Xu BX. 3D-multilayer simulation of microstructure and mechanical properties of porous materials by selective sintering. GAMM-Mitteilungen 2021;44:e202100017.

[33] Javili A, Chatzigeorgiou G, Steinmann P. Computational homogenization in magneto-mechanics. International Journal of Solids and Structures 2013;50:4197-216.

[34] Bleistein T, Reis M, Cheng X, Redenbach C, Diebels S, Jung A. Multiscale microsphere modelling of open-cell metal foams enriched by statistical analysis of geometric parameters. Mechanics of Materials 2020;142:103295.

[35] Fahlbusch NC, Becker W, Kolupaev VA, Geertz G. Nonlinear material behaviour and failure of closed-cell polymer foams. Acta Mechanica 2016;227:3113-21.

[36] Fahlbusch NC, Grenestedt JL, Becker W. Effective failure behavior of an analytical and a numerical model for closed-cell foams. International Journal of Solids and Structures 2016;97:417-30.

[37] Miyoshi T, Itoh M, Akiyama S, Kitahara A. ALPORAS aluminum foam: production process, properties, and applications. Advanced engineering materials 2000;2:179-83.

[38] Jang WY, Hsieh WY, Miao CC, Yen YC. Microstructure and mechanical properties of ALPORAS closed-cell aluminium foam. Materials Characterization 2015;107:228-38.

[39] Pourmoghaddam N, Kraus M, Schneider J, Siebert G. Relationship between strain energy and fracture pattern morphology of thermally tempered glass for the prediction of the 2D macro-scale fragmentation of glass. Glass Structures & Engineering 2019;4:257-75.

[40] Kraus MA. Machine Learning Techniques for the Material Parameter Identification of Laminated Glass in the Intact and Post-Fracture State. Doctoral dissertation. Bundeswehr University Munich, Munich, 2019.

[41] Chen Y, Das R, Battley M. Effects of cell size and cell wall thickness variations on the stiffness of closed-cell foams. International Journal of Solids and Structures 2015;52:150-64.

[42] Luo G, Xue P, Li Y. Experimental investigation on the yield behavior of metal foam under shear-compression combined loading. Science China Technological Sciences 2021;64:1412-22.

[43] Sun Y, Amirrasouli B, Razavi SB, Li Q, Lowe T, Withers P. The variation in elastic modulus throughout the compression of foam materials. Acta Materialia 2016;110:161-74.

[44] Shen J, Lu G, Ruan D. Compressive behaviour of closed-cell aluminium foams at high strain rates. Composites Part B: Engineering 2010;41:678-85.

[45] Schlimper R, Rinker M, Schäuble R. Prediction of material behaviour of closed cell rigid foams via mesoscopic modelling. Proceedings of the International Committee on Composite Materials Meeting: ICCM2009. p. 27-31.

[46] Stanzick H, Wichmann M, Weise J, Helfen L, Baumbach T, Banhart J. Process Control in Aluminum Foam Production Using Real-Time X-ray Radioscopy. Advanced Engineering Materials 2002;4:814-23.

[47] Ashby MF, Evans AG, Fleck NA, Gibson LJ, Hutchinson JW, Wadley HNG. Metal Foams: A Design Guide. Butterworth-Heinemann; 2000.

[48] Kováčik J, Marsavina L, Linul E. Poisson's ratio of closed-cell aluminium foams. Materials 2018;11:1904.

[49] Ramamurty U, Paul A. Variability in mechanical properties of a metal foam. Acta materialia 2004;52:869-76.

[50] Simone A, Gibson L. Effects of solid distribution on the stiffness and strength of metallic foams. Acta Materialia 1998;46:2139-50.

[51] Benouali AH, Froyen L, Dillard T, Forest S, N'guyen F. Investigation on the influence of cell shape anisotropy on the mechanical performance of closed cell aluminium foams using micro-computed tomography. Journal of materials science 2005;40:5801-11.

[52] Mondal D, Ramakrishnan N, Suresh K, Das S. On the moduli of closed-cell aluminum foam. Scripta Materialia 2007;57:929-32.

[53] Rakow JF, Waas AM. Size effects and the shear response of aluminum foam. Mechanics of Materials 2005;37:69-82.

[54] Gregorová E, Pabst W, Uhlířová T, Nečina V, Veselý M, Sedlářová I. Processing, microstructure and elastic properties of mullite-based ceramic foams prepared by direct foaming with wheat flour. Journal of the European Ceramic Society 2016;36:109-20.

[55] Rosendahl PL, Weißgraeber P. Modeling snow slab avalanches caused by weak-layer failure–Part 1: Slabs on compliant and collapsible weak layers. The Cryosphere 2020;14:115-30.

[56] Rosendahl PL, Weißgraeber P. Modeling snow slab avalanches caused by weak-layer failure–Part 2: Coupled mixed-mode criterion for skier-triggered anticracks. The Cryosphere 2020;14:131-45.

[57] Ke LL, Yang J, Kitipornchai S. Nonlinear free vibration of functionally graded carbon nanotube-reinforced composite beams. Composite Structures 2010;92:676-83.

[58] Katsikadelis JT. Dynamic Analysis of Structures. Academic press; 2020.

[59] Zai BA, Ahmad F, Lee CY, Kim TO, Park MK. Structural Optimization of Cantilever Beam in Conjunction with Dynamic Analysis. Journal of the Korean Institute of Gas 2011;15:31-6.